

Research Article

Mechanical Behavior and Its Influencing Factors on Engineered Cementitious Composite Linings

Zude Ding , Jiang Fu, Xiaoqin Li , and Xiafei Ji

Faculty of Civil Engineering and Mechanics, Kunming University of Science and Technology, Kunming 650500, China

Correspondence should be addressed to Xiaoqin Li; xiaoqin.li@foxmail.com

Received 12 January 2019; Accepted 16 July 2019; Published 14 August 2019

Academic Editor: Jean-Michel Bergheau

Copyright © 2019 Zude Ding et al. This is an open access article distributed under the Creative Commons Attribution License, which permits unrestricted use, distribution, and reproduction in any medium, provided the original work is properly cited.

A 1/5-scale model test was used to analyze and compare the mechanical responses of engineered cementitious composite (ECC) lining and traditional concrete lining under vertically concentrated loading. Test results indicate that the major failure mode of the lining cross section is controlled by tensile stress. ECC linings express better cracking control capability and deformation performance than the traditional concrete tunnel linings. On this basis, the effects of loading direction, material tensile properties, soil stiffness, and model size on the mechanical behavior of ECC and R/ECC linings were analyzed by numerical calculation. Parametric analysis shows that the failure modes of ECC and R/ECC linings along different load directions are caused by the loss of bearing capacity due to the formation of three plastic hinges. Lining damage under horizontal loading is more concentrated than those under vertical and oblique loading. Improving the tensile properties of ECC materials can help enhance the load capacity and deformability of linings. Soil stiffness obviously affects the postpeak deformation behavior of ECC linings, as shown by the sharp increase of the load-displacement curve with the increase of soil stiffness. The peak load and corresponding displacement of linings demonstrate nonlinear increase with the increase in model size.

1. Introduction

The main influencing factors of the mechanical behavior of traditional concrete lining under external loads include loading mode, soil stiffness, and material properties. The failure modes of linings are generally represented by structural failure caused by the plastic rotation of softening hinges, tensile failure caused by localised cracks, and material failure caused by concrete deterioration [1, 2]. In comparison with normal concrete (NC), fiber-reinforced concrete (FRC) can considerably improve the toughness and cracking control capability [3, 4] and effectively reduce the cracking of traditional concrete lining [5]. In recent years, FRC has been continuously used in tunnel engineering, especially in urban precast tunnel segments, and its mechanical behavior has attracted wide attention [6–10].

Experimental studies on the mechanical properties of steel fiber-reinforced concrete (SFRC) linings and precast segments have shown that the randomness of fiber distribution manifests a good crack control capability [8–12].

Moreover, corrosion hazard from using SFRC is considerably less than that from using traditional steel bars due to the short and discontinuous distribution of steel fibers [13], and the partial or total replacement of steel bars with steel fibers can increase the corrosion resistance of concrete structures. However, the chloride ion content of SFRC after cracking is nearly three times that of non-SFRC under wetting and drying cycles [14]. Therefore, non-SFRC lining has also received a widespread attention. A series of studies on the model tests of polypropylene fiber-reinforced concrete (PFRC) segments, steel-reinforced PFRC segments, and basalt FRC linings have shown that FRC linings have better loading capacity, deformation performance, and crack control capability than traditional concrete linings [15–18]. The fiber volume content of FRC is usually less than 2% in practice due to difficulties in their construction (e.g., steel fiber). Early cracking is somewhat reduced relative to conventional concrete, and material toughness is improved, but the strain-softening phenomenon continues to occur when effective stress exceeds tensile strength. After cracking,

the cracks immediately enter the localised expansion stage. In cases of high local stress (i.e., weak surrounding rock sections, active fault sections, and high-intensity seismic zones that are prone to large deformation), improving further the deformation performance of the lining is necessary. Polyvinyl alcohol fiber-engineered cementitious composite (PVA-ECC, hereafter referred simply as ECC) exhibits ultrahigh toughness, high tensile strength, and high cracking resistance and durability, but multiple fine cracks are generated under tensile loading [19–28]. The ultimate tensile strain of ECC can exceed 3%, which is more than 100 times that of NC, given the same strength grade; it also has remarkable strain-hardening characteristics under tensile and bending loads [19–22]. ECC can control crack widths within 50 μm under peak load by producing stable plurality of fine cracks [23], which suggests excellent durability given the effective inhibition of appearance and development of early shrinkage cracks [24]. The maximum tensile strain capacity of ECC is 20–50 times that of existing SFRC and PFRC [25, 26]. In recent years, ECC has been applied to ground structural components, such as beams and columns [27, 28], and preliminarily applied to underground and hydraulic structures [29–32]. Under uniaxial and cyclic loads, the coordinated action of PVA fibers and steel bars can enhance the load bearing and deformation capacities of pipelines [31], and the ECC was developed for the anti-faulting design of tunnels in active fault zones [32].

However, the lack of experimental data on the mechanical behavior and influencing factors of ECC lining limits its application in underground engineering. Here, the mechanical responses of ECC lining and steel-reinforced ECC (R/ECC) lining under concentrated vertical load are studied by using a 1/5-scale loading test and then compared with those of traditional NC lining and reinforced concrete (RC) lining. On the basis of reasonable descriptions on the nonlinear constitutive relation of ECC, numerical calculation models of the ECC and R/ECC linings were established, and the influences of loading directions, material mechanical parameters, soil stiffness, and model size on the mechanical behavior of the linings were analyzed.

2. Model Tests

2.1. Model of Testing Setup. The testing setup with a 1/5-scale lining model was developed by using an existing testing machine [33]. As shown in Figure 1, the model of testing setup includes a reaction steel support frame, electrohydraulic loading jacks, and equivalent subgrade setup. The reaction frame was assembled by M30 bolts with nine H-shaped steel members in 3950 mm (width) \times 2610 mm (height) \times 300 mm (thickness) dimension. This frame provided nine loading points along the lining. Amongst these loading points, a 300 kN electrohydraulic jack was installed in the lining vault for the vertically concentrated loading configuration, and the maximum stroke was 300 mm. The remaining loading points were simulated for the subgrade reaction by combining rubber plate and jack. The side of the rubber plates in contact with the lining was processed to realise a curve-shaped lining,

in which the size of the single rubber plate was 300 mm \times 300 mm, and plate thickness was 100 mm. The uniaxial compression test was performed to determine the elastic behavior of the rubber plate. The representative compression-deformation curve is shown in Figure 2. The rubber plate was bilinear under axial load. Compressive stiffness was 3.38 MN/m when compression deformation was lower than 20 mm, and then it reached 4.87 MN/m when compression deformation exceeded 20 mm. Both the results of the numerical simulation and prototype-loading tests showed that the deformation of the lining ring was lower than 20 mm. Therefore, the compression stiffness of the rubber plate was taken to be 3.38 MN/m. The equivalent soil stiffness was 27.9 MPa/m.

2.2. Model Test Contents. Four test conditions, particularly the loading tests of traditional NC lining, ECC lining, RC lining, and R/ECC lining, were considered in this experimental study. The lining damage caused by external loads can be generally attributed to loosening vertical soil pressure, horizontal plastic soil pressure, and unbalanced soil pressure, as shown in Figure 3. The vertically concentrated loading configuration was used in the test to simulate the case in which the lining was subjected to loosening vertical soil pressure, which is similar to the loading method described in the literature [1, 34]. If the influence of self-weight on the structure is ignored and the external load is concentrated, then prototype materials can be used for the model tests; notably, this technique is commonly used in modelling concrete structures [35]. Therefore, prototype materials were used to construct the lining models in this test.

2.3. Test Materials and Lining Members. The mix ratio of NC and ECC is given in Table 1. Uniaxial compressive strength was determined by testing the cubic specimens (150 mm \times 150 mm \times 150 mm) of NC and ECC cured for 28 days. The compressive strength values of the NC and ECC specimens were 28.2 and 35.3 MPa, respectively. An ECC dumbbell-type test piece was also constructed, and the axial direct tensile test of the ECC test piece was performed on a 10 kN electronic universal testing machine. The tensile stress-strain curve of the ECC is shown in Figure 4, from which strain-hardening characteristics are apparent. Peak tensile stress and strain were 3.1 MPa and 2.6%, respectively.

The lining member was constructed in accordance with the 1/5 scale of a common two-lane road tunnel lining in China, and its dimension was 2.3 m (width) \times 1.56 m (height) \times 80 mm (thickness). The lining width along the longitudinal direction was 300 mm. The reinforcement ratio of the prototype lining was 0.7%; hence, the reinforcement design was in accordance with the principle of the equal reinforcement ratio. After conversion, steel bars were added to the lining model. The diameters of the distributed steel bars were 4 mm@40 mm and 2 mm@50 mm. Figure 5 shows in detail the dimensions of the lining member and the reinforcement configuration.

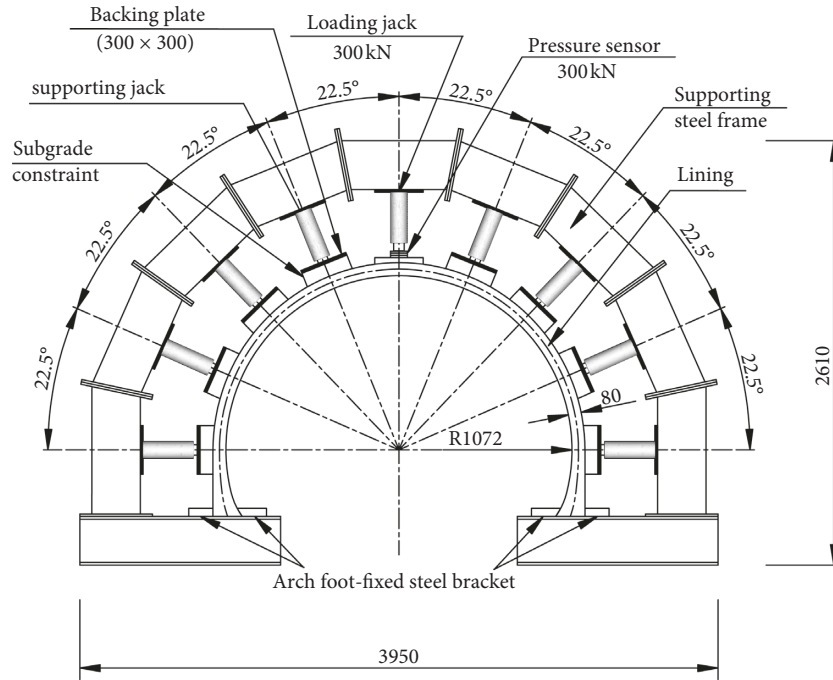


FIGURE 1: Schematic of the testing setup (unit: mm).

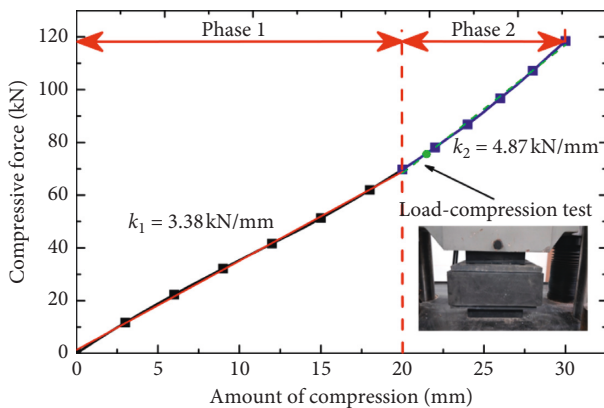


FIGURE 2: Compression deformation curve of the rubber plate.

2.4. *Sensor Arrangement and Testing Process.* The values of load, displacement, and strain during the loading process of the lining were collected by using pressure sensors, strain gauges, and displacement transducers (Figure 6). The displacement control loading mode with a loading rate of 0.5 mm/min was adopted. Crack width was measured in 5 mm increasing increments in the vault displacement setup. Crack distribution was also recorded until lining failure was reached.

3. Experimental Result Analysis

3.1. *Load-Displacement Response.* The load-displacement responses and the corresponding test results of the four linings are shown in Figure 7 and Table 2, respectively. The methods for determining yield load and failure load and their displacements are as follows: yield point represents

the farthest distance point from the line between the origin and peak points on the load-displacement curve, and the corresponding load and displacement are the yield load and its displacement, respectively [36], and 85% of the peak load is taken as the failure load, and the corresponding displacement is the failure displacement [37]. Ductility is an important property when evaluating lining deformation capacity. This study adopted the ductility calculation method defined in [37, 38], which is expressed as follows:

$$\mu = \frac{\Delta_u}{\Delta_y} \quad (1)$$

where Δ_u and Δ_y are the failure and yield displacements of the lining member, respectively.

As shown in Figure 7, the load-displacement curves of all the linings can be divided into three stages, namely, linear elasticity stage (OC), elastoplastic stage (CP), and failure stage (PF). The elastic stage represents the linear portion of the curve from the beginning of loading to the appearance of the cracking point. As microcracks develop, the slope of the load-displacement curve gradually decreases, which indicates reduction in lining stiffness until the peak load is reached. Lining deformation continuously increases with the development of additional cracks, and bearing capacity gradually decreases until the occurrence of breakage and crushing failure of the linings.

However, the load-displacement curves of the four linings differ significantly in each stage, as shown in Figure 7 and Table 2. The cracking load and corresponding displacement of the ECC lining were 1.23 and 1.79 times of those of the NC lining and 0.92 and 1.58 times of those of the RC lining, respectively. The cracking load of the

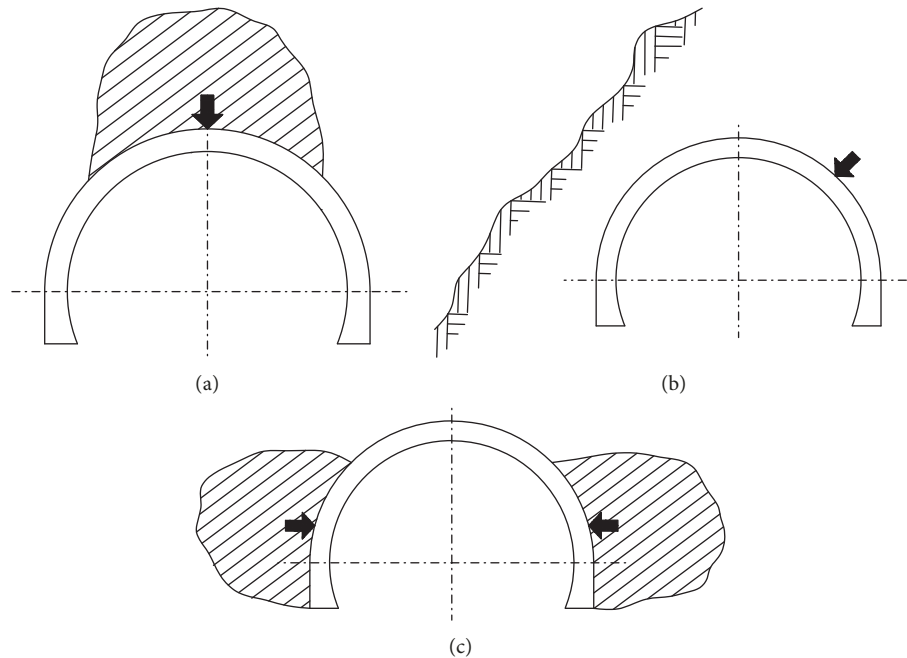


FIGURE 3: Common soil pressure modes of lining deformation and failure: (a) loosening vertical soil pressure; (b) horizontal plastic soil pressure; (c) unbalanced soil pressure.

TABLE 1: Mix proportion design of concrete (mass ratio).

Materials	Cement	Fly ash	Fine aggregate	Coarse aggregate	Water	Water reducer	Fiber
ECC	1.0	1.29	0.69	—	0.80	0.001	0.0532
NC	1.0	0.18	2.53	3.6	0.54	0.006	—

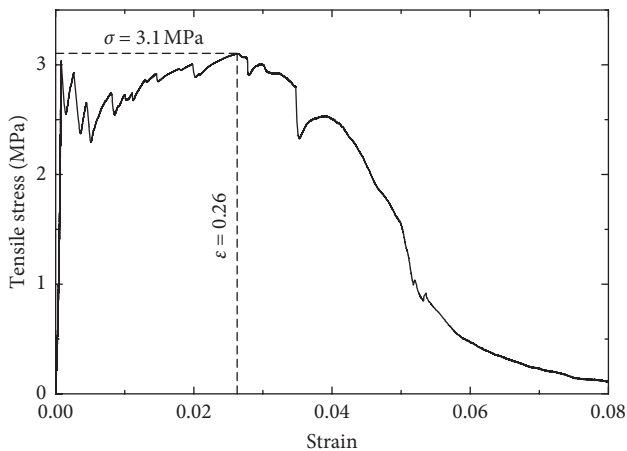


FIGURE 4: Uniaxial tensile stress-strain curve of ECC.

ECC lining was nearly the same as that of the RC lining, but cracking displacement was larger than that of traditional concrete linings. The cracking load and corresponding displacement of the R/ECC lining were obviously larger than those of the three abovementioned linings. On the basis of the results, ECC can delay the generation of microcracks and ECC and R/ECC linings have good cracking control capacity. The peak load of the ECC lining was 29.2% higher than that of the NC lining,

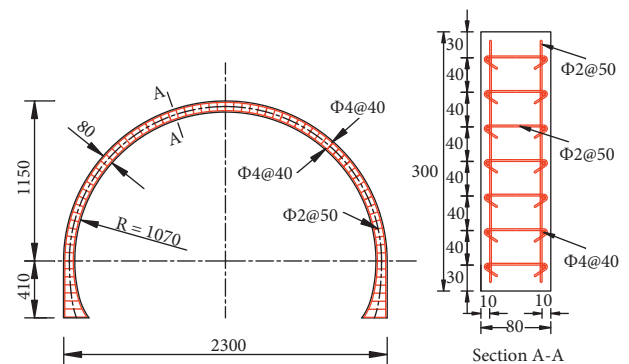


FIGURE 5: Geometry and reinforcement configuration of the lining member (unit: mm).

which was close to that of the RC lining (the difference was less than 10%). Moreover, the peak load of the R/ECC lining was 33.7% higher than that of the RC lining. The ECC and R/ECC linings achieved the same or even better load capacity compared with the traditional linings. Unlike the load-displacement curves of the traditional linings, those of the ECC and R/ECC linings do not appear with a sudden drop at the failure stage, thereby indicating good postpeak deformation performance. According to the calculation results of the displacement ductility factor, the ductility of the ECC and R/ECC linings was 27.5% and

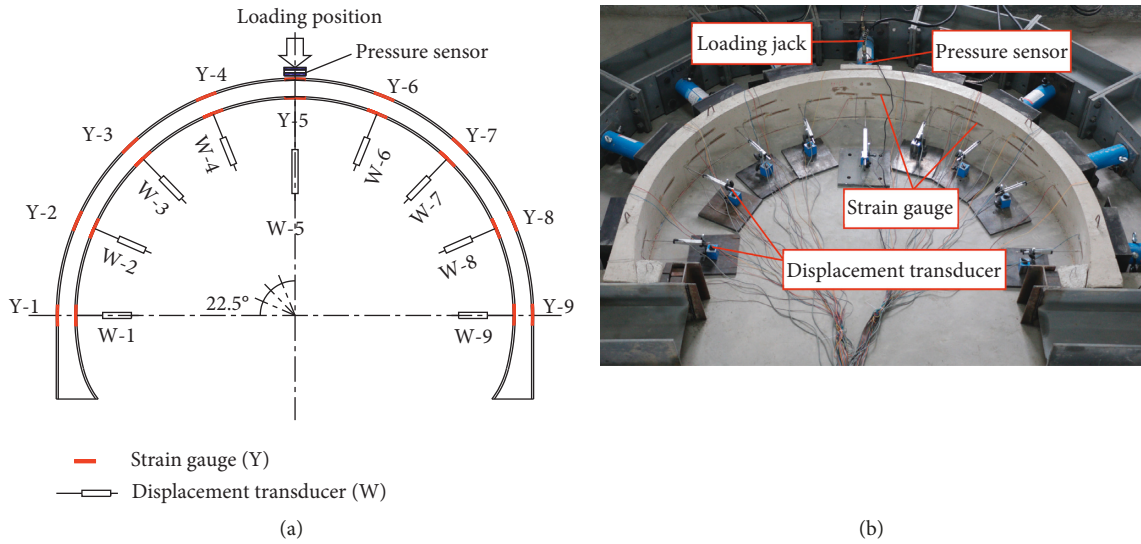


FIGURE 6: Test arrangements: (a) schematic; (b) photo.

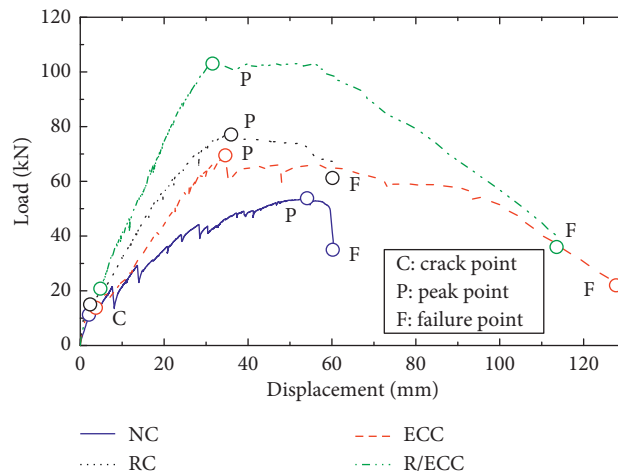


FIGURE 7: Load-displacement curves.

TABLE 2: Test results of lining members.

Linings	Crack initiation		Yield		Peak		Failure		Ductility factor
	Displacement (mm)	Load (kN)							
NC	2.09	11.24	23.34	39.62	54.07	53.81	59.63	48.84	2.55
RC	2.37	14.99	19.72	54.22	35.97	77.11	60.13	65.56	3.05
ECC	3.74	13.78	24.41	54.73	34.59	69.52	79.49	59.08	3.26
R/ECC	4.82	20.77	20.08	72.56	31.54	103.06	71.21	87.67	3.55

38.8% higher than that of the NC lining and 6.8% and 16.3% higher than that of the RC lining, respectively, which implies consistently better ductility.

3.2. *Crack and Failure Patterns.* Figure 8 shows the crack distribution and failure patterns of the four linings. In the figure, \circ symbolises tensile cracking, \bullet symbolises compression fracture, the expression $1 - x$ represents the order of

crack appearance, and the broken lines represent lining deformation. The major failure mode of all the linings was controlled by tensile stress under vertically concentrated loading. Firstly, initial cracking was observed in the lining crown. Then, as displacement loading increased, the outer lining spandrel began to show tensile cracks. Finally, the cracks expanded gradually until the concrete outside the crown and inside the spandrel collapsed, and the lining became completely destroyed.

Although the failure patterns of the four linings were similar (Figure 8), their crack distributions and propagation differed. The NC and RC linings presented only one main crack in the lining crown and the left and right spandrels, and smeared cracking was not found. By contrast, the ECC and R/ECC linings showed multiple microcracks in the crown during the loading process. As displacement increased, many small cracks appeared on the outside of the spandrels. The ECC lining exhibited multiple crack distributions due to the crack resistance of fibers. Crack depth and width increased slowly, thereby indicating desirable crack control and dispersion capability, particularly for the R/ECC lining. The concrete-peeling phenomena occurred with the crushing of the spandrels of the NC and RC linings, whereas the ECC and R/ECC linings did not peel off, which implies an obvious antifracking effect.

$$\sigma = \begin{cases} E_c \varepsilon, & 0 \leq \varepsilon < \frac{\varepsilon_{c0}}{3}, \\ \frac{f_c}{3} \left[1 + 4 \left(\frac{\varepsilon - (\varepsilon_{c0}/3)}{\varepsilon_{c0} - (\varepsilon_{c0}/3)} \right) - 2 \left(\frac{\varepsilon - (\varepsilon_{c0}/3)}{\varepsilon_{c0} - (\varepsilon_{c0}/3)} \right)^2 \right], & \frac{\varepsilon_{c0}}{3} \leq \varepsilon < \varepsilon_{c0}, \\ f_c \left[1 - \left(\frac{\varepsilon - (\varepsilon_{c0}/3)}{\varepsilon_{c0} - (\varepsilon_{c0}/3)} \right)^2 \right], & \varepsilon_{c0} \leq \varepsilon < \varepsilon_{cu}, \end{cases} \quad (2)$$

$$\varepsilon_{c0} = \frac{5f_c}{3E_c},$$

$$\varepsilon_{cu} = \frac{3G_c}{2f_c h} + \varepsilon_{c0},$$

where E_c , f_c , and G_c are Young's modulus, the compressive strength, and the compressive fracture energy of ECC, respectively. For planar elements, h was set as $h = \sqrt{2A}$, where A is the finite element area.

The tension behavior of ECC can be described by a multilinear model (Figure 9(b)) [43, 44]. The calculation parameters of ECC are shown in Table 3.

4.2. Steel Material Modelling. The von Mises multilinear model [45] was adopted for steel bar characterisation. The stress-strain curve and calculation parameters of the steel bar are shown in Figure 10 and Table 4, respectively.

4.3. Structural Model. The tunnel lining was discretised by referring to four-node quadrilateral plane stress elements. The line pressure interface element was used to simulate the contact between the lining and the loading plate and subgrade constraint outside the tunnel lining. The embedded steel bar element was used to simulate the steel bar (i.e., regardless of the bond slip between the steel bar and the concrete), and the fixed restraint was used to simulate the

4. Numerical Model

The loading and failure processes of the ECC and R/ECC linings were simulated by using the FEM software Diana (version 10.2) [39]. The size of the lining models, the boundary conditions, and the loading directions were consistent with the test condition. The total strain-rotating crack model used for ECC modelling in this study is suitable for limit state analysis [1, 40–42].

4.1. ECC Material Modelling. The compression behavior of ECC was described by a parabolic model derived from fracture energy (Figure 9(a)) [42]. The compressive stress-strain relationship can be expressed as follows:

bottom support. The finite element calculation model is shown in Figure 11.

5. Verification of Numerical Model

A plane stress model was used in this study, considering that the test involved lining loading in the plane stress state. The calculated load-carrying capacity of the lining was significantly larger than the experimental value based on the soil stiffness values determined by the rubber compression test. This finding can be attributed to the range of the rubber plate that did not cover the entire lining circumference (i.e., the proportion was 75%) and the soil stiffness conversion method that approximates equivalent stiffness at 20 MPa/m. The numerical results based on equivalent stiffness were found to be in good agreement with the test results. Therefore, equivalent stiffness was adopted in the calculation. Then, the calculation results of the ECC lining with mesh sizes of 2, 5, and 10 mm were compared to eliminate the influence of mesh size. The peak loads and the shapes of the load-displacement curves of the three mesh sizes were close to one another. However, in consideration of computational efficiency and simulation

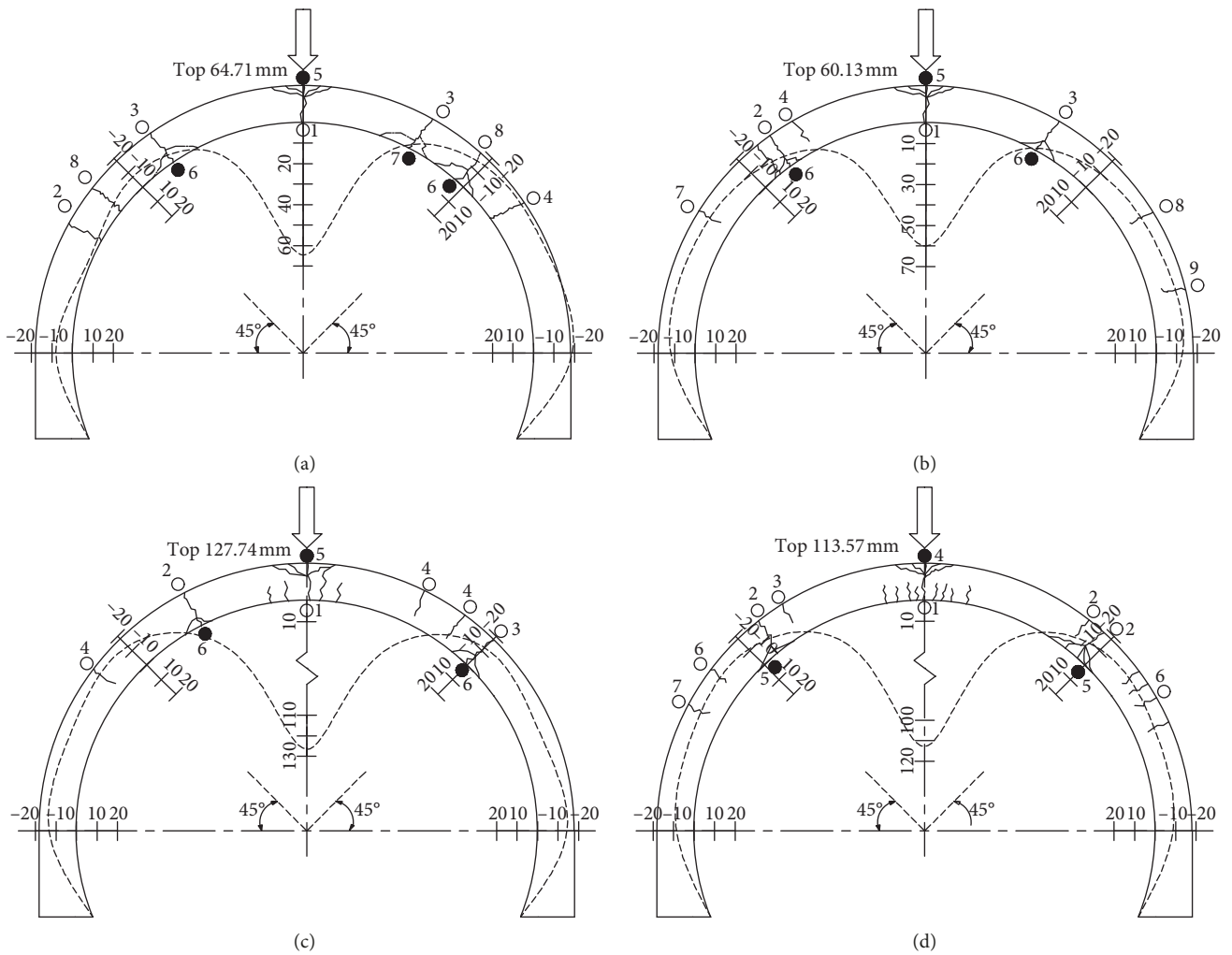


FIGURE 8: Cracking, deformation, and failure patterns of the lining members: (a) NC lining; (b) RC lining; (c) ECC lining; (d) R/ECC lining.

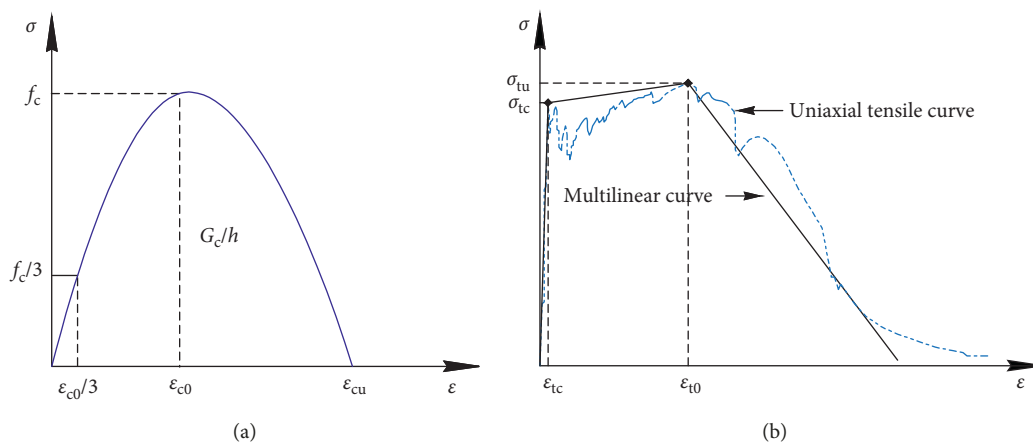


FIGURE 9: ECC constitutive relationship: (a) ECC in compression; (b) ECC in tension.

effect, the 5 mm mesh size was adopted in subsequent calculation.

In order to verify the reliability of the FE models, the FE results and experimental results were carefully compared, and the findings were as follows:

- (1) The test and modelling results of the load-displacement responses of the ECC and R/ECC linings (Figure 12) showed that the shape of the load-displacement curves of the modelling was similar as those from tests. The simulations can express the

TABLE 3: Physical and mechanical parameters of ECC.

Elastic modulus, E (GPa)	Poisson's ratio, μ	Compressive strength, f_c (MPa)	Yield tensile stress, σ_{tc} (MPa)	Ultimate tensile stress, σ_{tu} (MPa)	Yield tensile strain, ϵ_{tc}	Peak tensile strain, ϵ_{tu}
15	0.2	35.3	2.6	3.1	0.001	0.026

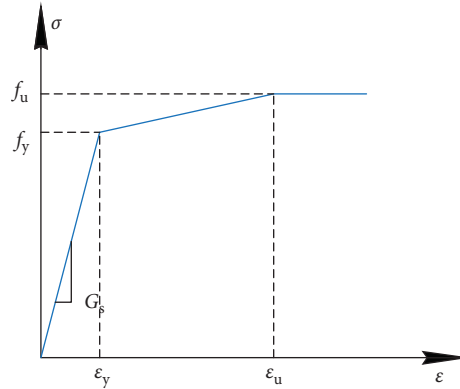


FIGURE 10: Stress-strain curve of steel.

TABLE 4: Physical and mechanical parameters of steel.

Elastic modulus, E_s (GPa)	Poisson's ratio, μ	Yield strength, f_y (MPa)	Yield strength tensile strain, ϵ_y	Ultimate strength, f_u (MPa)	Ultimate tensile strain, ϵ_u
200	0.2	300	0.01675	420	0.025

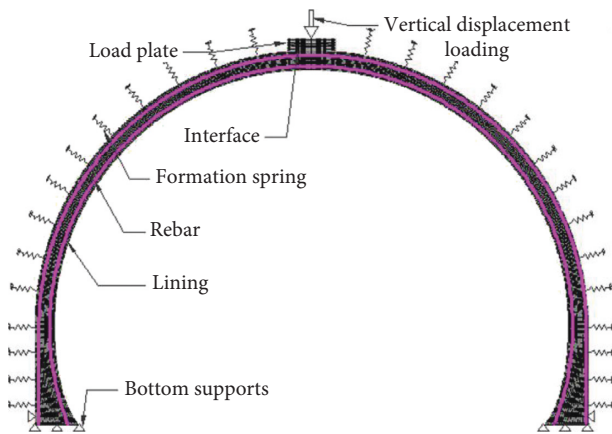


FIGURE 11: Schematic of the calculation model.

three stages of the load-displacement curves and the strain-hardening characteristics after reaching the peak loads, which showed the similar tendency as the tests results.

- (2) For the ECC and R/ECC linings, the peak loads of the modelling results were 70.8 kN and 112.0 kN, respectively, which were 1.8% and 8.7% higher than that of the tested values separately. The peak loads from the FE models were just slightly higher than the tested values, of which the differences were all under 10%. Meanwhile, the areas under the load-displacement curves of the FE models and the tests are

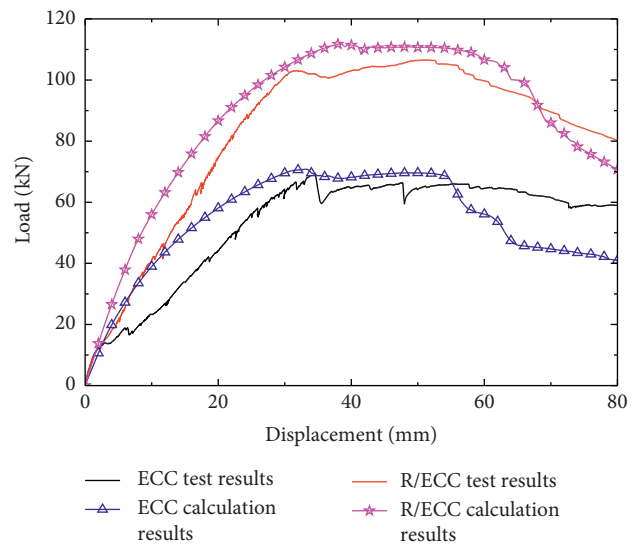


FIGURE 12: Load-displacement curves of ECC and R/ECC linings.

very close to each other. These all indicate that the numerical results were very close to the test data.

- (3) The failure patterns from the modelling (Figure 13) and the experimental failure patterns (Figure 8) could be compared, which showed that the failure patterns from FE and tests were consistent and the failure locations were identical both for ECC and R/ECC linings.

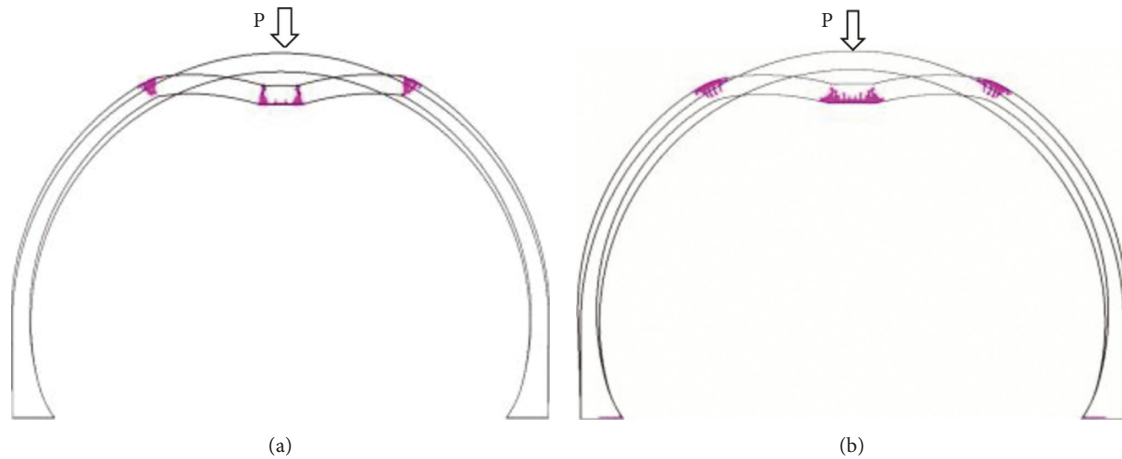


FIGURE 13: Deformation shapes and crack distribution of the linings: (a) ECC; (b) R/ECC.

According to the discussions listed above, the current FE models can accurately simulate the mechanical behaviors of the ECC and R/ECC linings under vertical concentrated loads.

6. Parametric Analysis

From the above finite element calculation models of the ECC and R/ECC linings, the following four factors are discussed: (1) load direction; (2) tensile stress and strain parameters of ECC; (3) soil stiffness; (4) size effect. The cases considered for parametric analysis are shown in Table 5.

6.1. Load Directions. Vertical (90°), oblique (45°), and horizontal (0°) loading directions were used to simulate three different soil pressures (Figure 3). The load-displacement responses of the ECC and R/ECC linings along different loading directions are shown in Figure 14. The curves of load-carrying capacity, ductility, and initial stiffness of the linings along different load directions are shown in Figure 15, and the lining failure modes are shown in Figure 16.

The load-displacement responses of the ECC and R/ECC linings were similar, and the differences in load capacity and initial stiffness were minimal under 90° and 45° loads (Figures 14 and 15). For the initial secant stiffness, the load capacity of the linings under 0° load was larger than those under 90° and 45° loads, the failure displacement was smaller, and the damage location was more concentrated due to the restriction of the fixed constraint at the bottom. Relative to the load capacities under 90° and 45° loads, the ECC lining under 0° load increased by 38% and 33% and initial stiffness increased by 5.5 and 6.1 times, respectively. Meanwhile, the load capacity of the R/ECC lining increased by 28% and 23%, and initial stiffness increased by 5.1 and 5.5 times, respectively (Figure 15). The ductility factor results indicate that load directions can affect the ductility of linings, and 90° and 0° loads have good ductility performances.

The failure modes of the ECC and R/ECC linings were similar along different load directions (Figures 13 and 16), and they were characterised by the formation of three plastic

hinges that led to the loss of load capacity of the lining structure. The R/ECC lining exhibited more distributed cracks than the ECC lining. This finding indicates that steel bars can help reduce stress concentration and subsequently lead to better crack control capability.

6.2. Tensile Stress and Strain Parameters of ECC. The tensile properties of ECC can be reflected by the yield and peak tensile stress and the corresponding tensile strain. Here, yield ϵ_{tc} and peak tensile strain ϵ_{tu} were kept constant, whilst yield tensile stress σ_{tc} and peak tensile stress σ_{tu} were changed in the calculation. The stress variable quantity can be expressed as $\Delta\sigma = 0.5$ MPa (calculation cases 7–14 in Table 5), where the plus sign represents “increase” and the minus sign represents “decrease.” Moreover, the effects of ECC tensile properties on the mechanical behavior of the linings were investigated by referring to the remaining stress value constant and by changing only the peak strain (calculation conditions 15–22 in Table 5). The load capacity and ductility of the ECC and R/ECC linings with different tensile properties are shown in Figure 17.

With the increase in ECC tensile strength, the load-carrying capacity and ductility of the two linings increased linearly although the increase in ductility was sharp and thus more apparent (Figure 17(a)). When the peak tensile stress of ECC increased from 3.1 MPa to 3.6 MPa, the bearing capacities of the ECC and R/ECC linings increased by 5.9% and 2.1% and ductility increased by 13.0% and 10.8%, respectively. The ultimate bearing capacity and ductility factor of the R/ECC lining were higher than those of the ECC lining, which indicates that adding steel bars can improve the mechanical performance of ECC linings.

The ultimate bearing capacity increased linearly, whereas ductility increased nonlinearly, with the increase in ECC peak tensile strain (Figure 17(b)). For each 0.01ϵ increase in peak tensile strain, the load capacities of the ECC and R/ECC linings increased by 38% and 20%, respectively. When the peak tensile strain increased from 0.01 to 0.05, the displacement ductility factors of the two linings increased 1.7

TABLE 5: Calculation cases.

Cases	Load directions	Tensile stress increment of ECC, $\Delta\sigma_t$ (MPa)	Peak strain of ECC, ε_{tu}	Soil stiffness, K_{soil} (MPa/m)	Size scale
1~6	90°, 45°, 0°	0	0.026	20	1/5
7~14	90°	-0.5, 0, 0.5, 1.0	0.026	20	1/5
15~22	90°	0	0.01, 0.02, 0.026, 0.05	20	1/5
23~34	90°	0	0.026	0, 20, 50, 150, 400, 850	1/5
35~40	90°	0	0.026	20	1/5, 1/2, 1/1
41~52	90°	0	0.026	0, 20, 50, 150, 400, 850	1/1

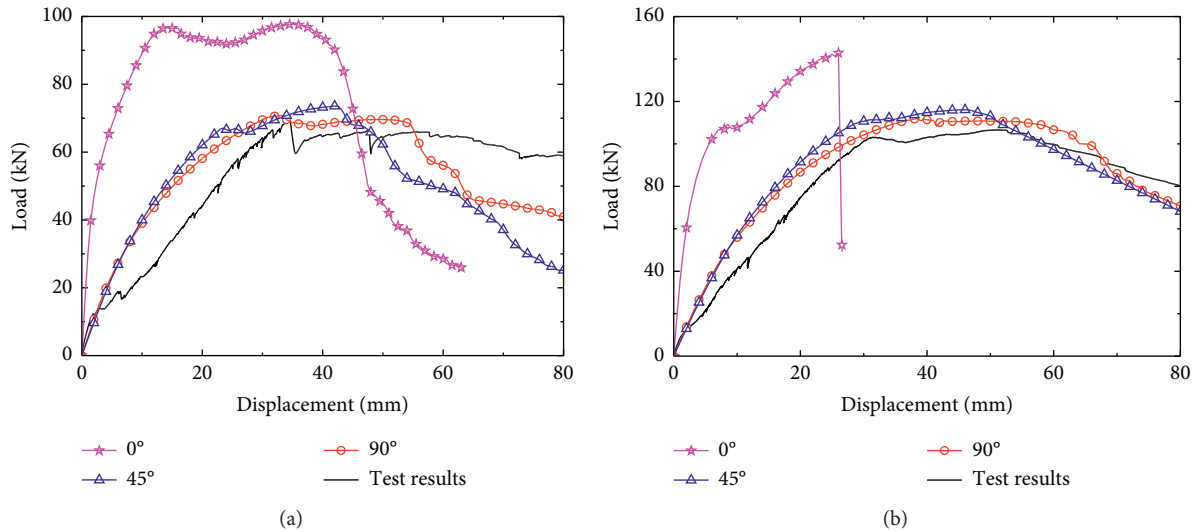


FIGURE 14: Load-displacement curves of ECC and R/ECC linings along different loading directions: (a) ECC; (b) R/ECC.

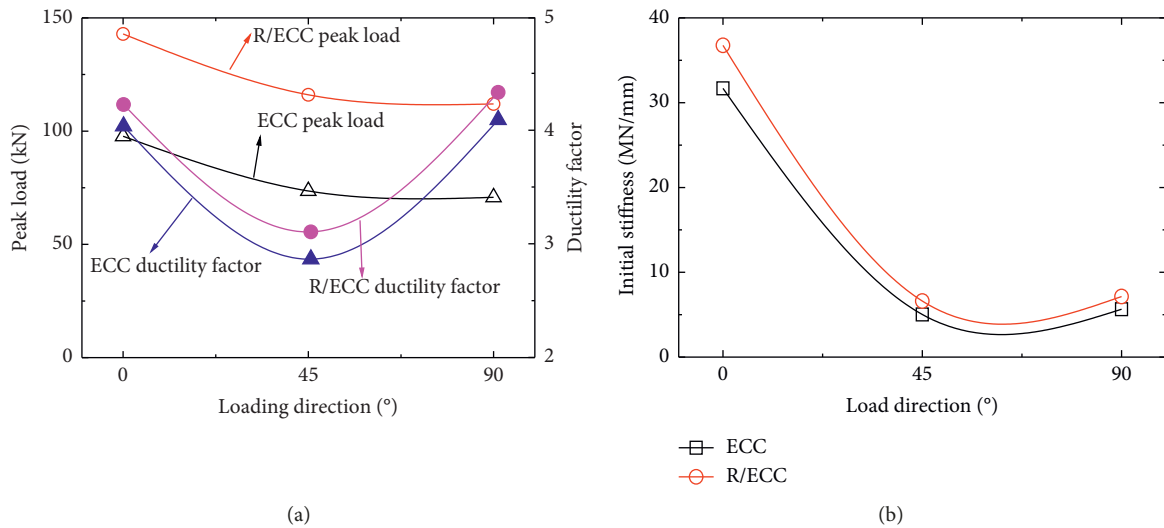


FIGURE 15: Load capacity, ductility, and initial stiffness-load direction curves: (a) peak load and displacement ductility factor; (b) initial stiffness.

times. Thus, enhancing the tensile properties of ECC can significantly improve the mechanical and deformation performances of the structure.

6.3. *Soil Stiffness.* Soil stiffness exerts a significant influence on the mechanical behavior of tunnel linings [1]. Here, the

mechanical properties of the ECC and R/ECC linings under different surrounding rock conditions were analyzed, and six cases of varying soil stiffness conditions were used for the simulation, including the recommended values of elastic resistance factors of surrounding rocks at Grades III–V [46].

The changes in ECC linings were consistent with those in R/ECC linings when soil stiffness increased. Load-

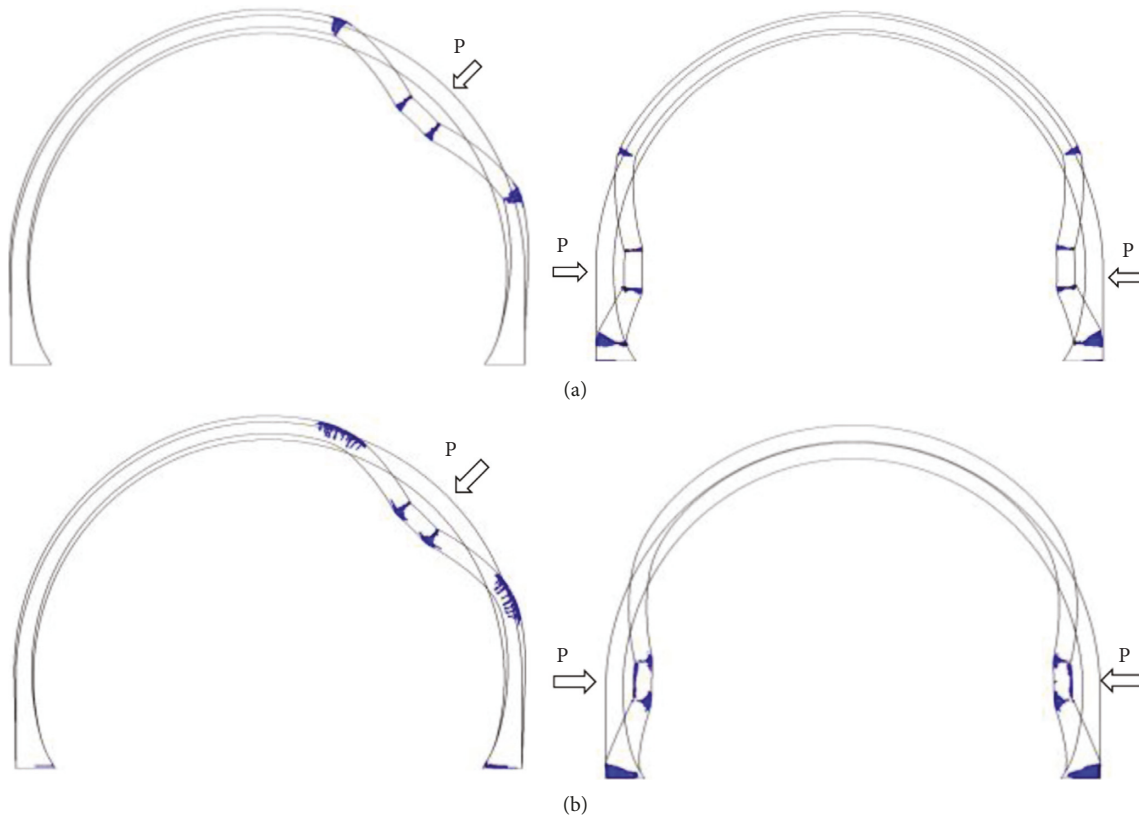


FIGURE 16: Lining failure modes along different loading directions: (a) ECC; (b) R/ECC.

displacement appears as a sharp curve with the increase of soil stiffness, which indicates that soil stiffness significantly affects the postpeak deformation behavior of linings. The changes in load capacity under different soil stiffness conditions can be presented as the three-stage law of rapid increase, slow down, and stability (Figure 18). Soil stiffness increased from 0 MPa/m (unconstrained) to 50 MPa/m, and the load capacities of the ECC and R/ECC linings increased by 6.92 and 4.56 times, respectively. When soil stiffness increased from 50 MPa/m to 400 MPa/m, the load capacities increased by 1.36 and 1.30 times. When soil stiffness increased from 400 MPa/m to 850 MPa/m, the load capacities increased by 3.8% and 3.6% only. The varying soil stiffness significantly influenced the load-carrying capacity of the linings when soil stiffness was small. However, the influence on load capacity gradually weakened when soil stiffness was large.

The ductility of the linings decreased rapidly with the increase of soil stiffness, which indicates strong subgrade constraint that can limit the effects of ECC anticracking and toughening. The secant stiffness of the linings was increased, but toughness was weakened (Figure 19(a)). Subsequently, ductility slightly increased with the increase of soil stiffness, which implies that the influence of soil stiffness on ductility is minimal when the surrounding rock conditions are relatively good. This finding may be explained by the tunnel lining failure in good rock condition that was controlled by compressive stress, and ductility was mainly affected by the compressive properties of materials [1]. As shown in

Figure 19(b), the initial stiffness of the linings exhibits a variation law consistent with load capacity having increasing soil stiffness.

6.4. Size Effect. The material parameters were unchanged to distinguish the size effect on lining structural response. Different sizes of tunnel linings with scale ratios of 1 : 1 (full size), 1 : 2, and 1 : 5 were investigated.

As shown by the load-displacement curves in Figure 20, the ascending branch is relatively mild and the descending branch is steep, which imply brittle response as the model size is increased. The peak loads and their corresponding displacements increased nonlinearly. The curves of lining load capacity, ductility, and initial stiffness with soil stiffness in full size are shown in Figure 21. The influence of soil stiffness on the mechanical behavior of full-sized lining can be divided into two stages. Firstly, when the soil stiffness increased from 0 MPa/m to 150 MPa/m, the bearing capacities of the ECC and R/ECC linings increased by 9.7 and 6.3 times, the initial secant stiffness increased by 10.0 and 8.7 times, and ductility decreased by 31.6% and 29.0%, respectively. The findings on soil stiffness demonstrate a significant effect on the mechanical behavior of the linings. Secondly, when soil stiffness increased from 150 MPa/m to 850 MPa/m, the bearing capacities of the two linings increased by 3.7% and 3.0% only and initial secant stiffness increased by 12.6% and 12.9%, respectively. The changes in soil stiffness indicate minimal effects on the linings.

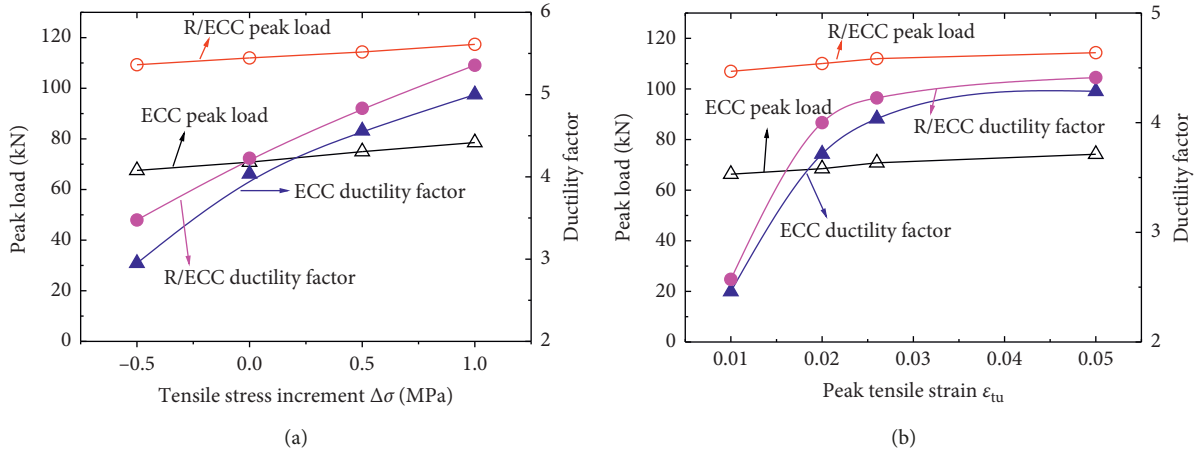


FIGURE 17: Mechanical behavior of linings with different tensile properties of ECC: (a) influence of $\Delta\sigma$; (b) influence of ϵ_{tu} .

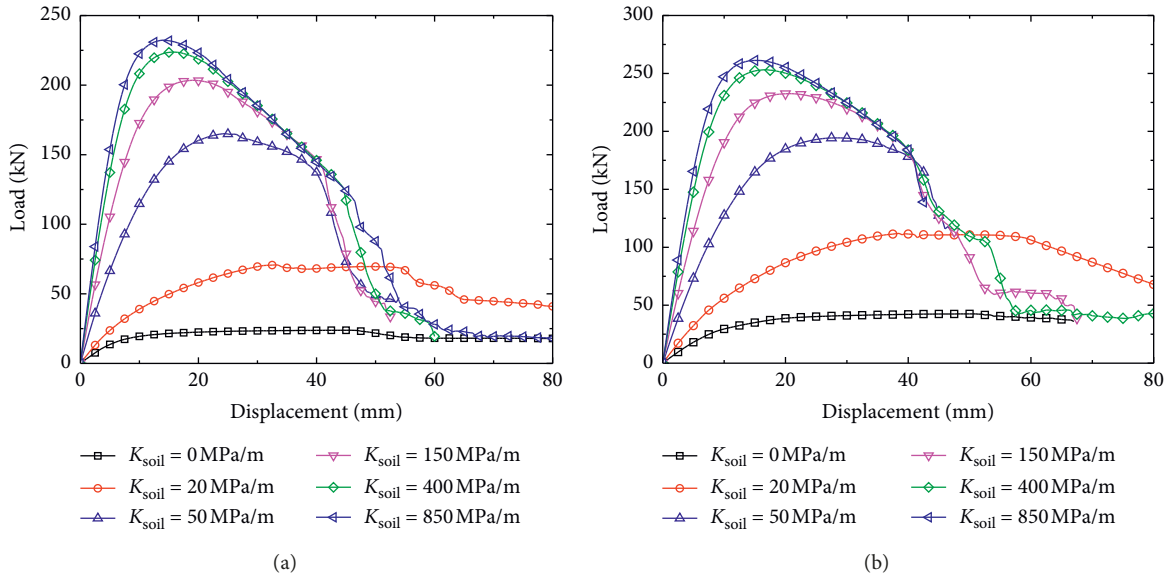


FIGURE 18: Load-displacement curves under different soil stiffness conditions: (a) ECC; (b) R/ECC.

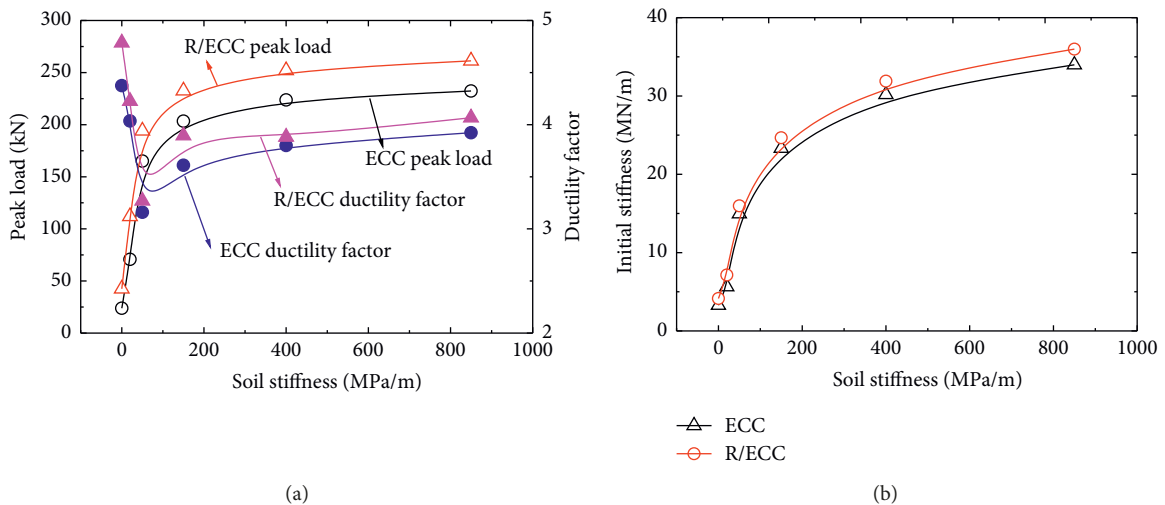


FIGURE 19: Lining load capacity, ductility, and initial stiffness-soil stiffness curves: (a) peak load and displacement ductility factor curves; (b) initial stiffness.

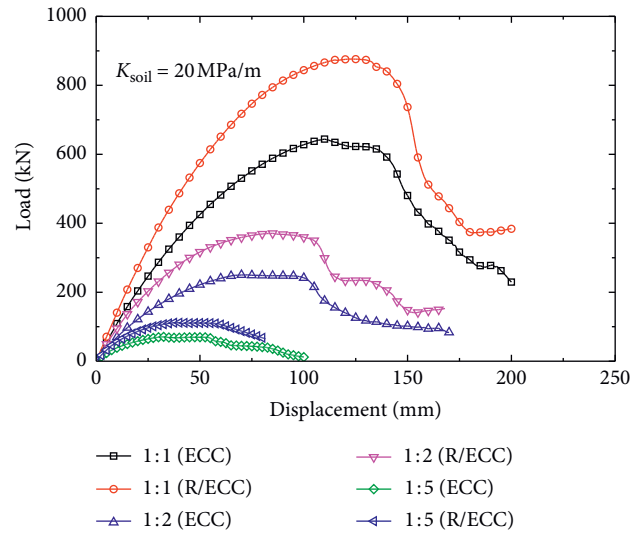


FIGURE 20: Load-displacement curves under different sizes of linings.

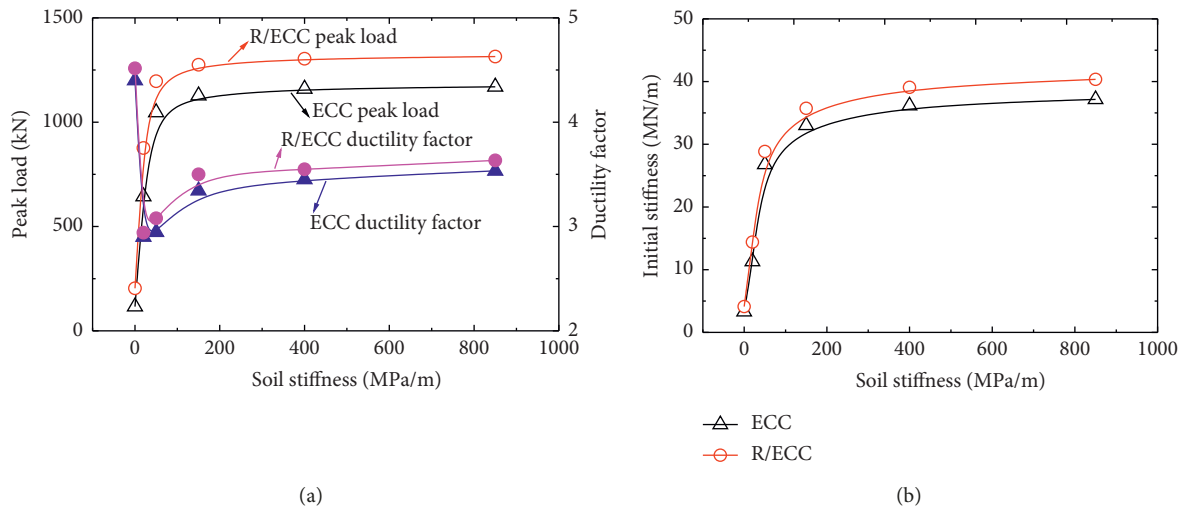


FIGURE 21: Lining load capacity, ductility, and initial stiffness-model size curves: (a) peak load and displacement ductility factor; (b) initial stiffness.

7. Conclusions

In this study, 1/5-scale model tests of four types of tunnel linings were performed under vertical concentrated load conditions, and the mechanical responses of the linings were determined. The influences of load direction, material tensile properties, soil stiffness, and model size on the mechanical behavior of the linings were analyzed on the basis of numerical simulations. The following conclusions can be drawn:

- (1) The major failure of the four linings is controlled by tensile stress in the lining cross section, which then contributes the superhigh toughness and crack resistance characteristics of ECC and its crack control capability. Moreover, the deformation performance and nonstripping capability of the ECC lining is superior to those of traditional NC and RC linings.

Compared with other three types of linings, the R/ECC lining demonstrates better cracking control capability, load-carrying capacity, and ductility.

- (2) By comparing the results of FE models and tests, the current ECC and R/ECC lining FE models are reliable, which can be used to analyze the stress and deformation characteristics of the linings under vertical concentrated loads.
- (3) The failure modes of the ECC and R/ECC linings along different load directions are all caused by the loss of load capacity due to the formation of three plastic hinges, but the damaged parts of the linings under horizontal loading are prominently concentrated. The linings exhibit different load-displacement responses towards the different load directions, and horizontal loading has manifested high load capacity and initial stiffness.

- (4) Improving the tensile properties of ECC materials can help improve the mechanical performances of tunnel linings, especially their ductility.
- (5) Loads and displacements appear as sharp curves with the increase of soil stiffness, which indicates that soil stiffness significantly affects the postpeak deformation behavior of linings. Load capacity under different soil stiffness conditions can be presented as the three-stage law of rapid increase, slow down, and stability. The anticracking and toughening effects of ECC are limited by strong constraints.
- (6) The peak load and the corresponding displacement of the linings increase nonlinearly as the model size is increased. The soil stiffness of 150 MPa/m is taken as the boundary in this study. The influence of soil stiffness on the mechanical behavior of the full-sized lining is observable in two stages. When soil stiffness is less than 150 MPa/m, the influence on the lining structure is significant. When the value is reached, soil stiffness starts to exhibit minimal effects.
- (7) The paper provides a case study on the application of ECC in tunnel engineering. More test and model work need to be done to evaluate mechanical properties of the linings with ECC application.

Data Availability

The data in figures and tables used to support the findings of this study are included within the article.

Conflicts of Interest

The authors declare that they have no conflicts of interest.

Acknowledgments

This research was supported by the National Natural Science Foundation of China (Grant nos. 51768028, 51308270, and 51308271)

References

- [1] W. He, Z. Wu, Y. Kojima, and T. Asakura, "Failure mechanism of deformed concrete tunnels subject to diagonally concentrated loads," *Computer-Aided Civil and Infrastructure Engineering*, vol. 24, no. 6, pp. 416–431, 2009.
- [2] H. M. Chen, H. S. Yu, and M. J. Smith, "Physical model tests and numerical simulation for assessing the stability of brick-lined tunnels," *Tunnelling and Underground Space Technology*, vol. 53, pp. 109–119, 2016.
- [3] N. Banthia and R. Gupta, "Influence of polypropylene fiber geometry on plastic shrinkage cracking in concrete," *Cement and Concrete Research*, vol. 36, no. 7, pp. 1263–1267, 2006.
- [4] T. Ayub, N. Shafiq, and M. F. Nuruddin, "Mechanical properties of high-performance concrete reinforced with basalt fibers," *Procedia Engineering*, vol. 77, pp. 131–139, 2014.
- [5] A. Inokuma and S. Inano, "Road tunnels in Japan: deterioration and countermeasures," *Tunnelling and Underground Space Technology*, vol. 11, no. 3, pp. 305–309, 1996.
- [6] B. Chiaia, A. P. Fantilli, and P. Vallini, "Combining fiber-reinforced concrete with traditional reinforcement in tunnel linings," *Engineering Structures*, vol. 31, no. 7, pp. 1600–1606, 2009.
- [7] A. D. L. Fuente, P. Pujadas, A. Blanco, and A. Aguado, "Experiences in Barcelona with the use of fibers in segmental linings," *Tunnelling and Underground Space Technology*, vol. 27, no. 1, pp. 60–70, 2012.
- [8] G. Meng, B. Gao, J. Zhou, G. Cao, and Q. Zhang, "Experimental investigation of the mechanical behavior of the steel fiber reinforced concrete tunnel segment," *Construction and Building Materials*, vol. 126, pp. 98–107, 2016.
- [9] S. Abbas, A. M. Soliman, and M. L. Nehdi, "Experimental study on settlement and punching behavior of full-scale RC and SFRC precast tunnel lining segments," *Engineering Structures*, vol. 72, no. 1, pp. 1–10, 2014.
- [10] M. L. Nehdi, S. Abbas, and A. M. Soliman, "Exploratory study of ultra-high performance fiber reinforced concrete tunnel lining segments with varying steel fiber lengths and dosages," *Engineering Structures*, vol. 101, pp. 733–742, 2015.
- [11] M. J. Avnani, A. Hoseini, S. Vahdani, and A. D. L. Fuente, "Numerical-aided design of fiber reinforced concrete tunnel segment joints subjected to seismic loads," *Construction and Building Materials*, vol. 170, pp. 40–54, 2018.
- [12] S. Carmona, C. Molins, A. Aguado, and F. Mora, "Distribution of fibers in SFRC segments for tunnel linings," *Tunnelling and Underground Space Technology*, vol. 51, pp. 238–249, 2016.
- [13] S. U. Balouch, J. P. Forth, and J.-L. Granju, "Surface corrosion of steel fibre reinforced concrete," *Cement and Concrete Research*, vol. 40, no. 3, pp. 410–414, 2010.
- [14] J. Zhang, H. T. Zhong, C. X. Ju et al., "Comparative study on Cl⁻ penetration in cracked high ductility and low shrinkage material and steel fiber concrete," *Journal of Building Materials*, vol. 15, no. 2, pp. 151–157, 2012.
- [15] A. Conforti, G. Tiberti, G. A. Plizzari, A. Caratelli, and A. Meda, "Precast tunnel segments reinforced by macro-synthetic fibers," *Tunnelling and Underground Space Technology*, vol. 63, pp. 1–11, 2017.
- [16] K. Behfarnia and A. Behravan, "Application of high performance polypropylene fibers in concrete lining of water tunnels," *Materials & Design*, vol. 55, pp. 274–279, 2014.
- [17] G. Y. Cui, D. Y. Wang, S. Z. Ni et al., "Model tests on bearing characteristics of basalt fiber-reinforced concrete tunnel linings," *Chinese Journal of Geotechnical Engineering*, vol. 39, no. 2, pp. 311–318, 2017.
- [18] P. Jain and T. Chakraborty, "Numerical analysis of tunnel in rock with basalt fiber reinforced concrete lining subjected to internal blast load," *Computers and Concrete*, vol. 21, no. 4, pp. 399–406, 2018.
- [19] V. C. Li, "Engineered cementitious composites-tailored composites through micromechanical modeling," in *Fiber Reinforced Concrete: Present and the Future*, N. Banthia, A. Bentur, and A. Mufti, Eds., vol. 1, no. 3, pp. 64–97, Canadian Society for Civil Engineering, Montreal, Canada, 1998.
- [20] V. C. Li, S. X. Wang, and C. Wu, "Tensile strain-hardening behavior of PVA-ECC," *ACI Materials Journal*, vol. 98, no. 6, pp. 483–492, 2001.
- [21] S. L. Xu and H. D. Li, "Uniaxial tensile experiments of ultra-high toughness cementitious composite," *China Civil Engineering Journal*, vol. 9, pp. 32–41, 2009.
- [22] J. H. Yu and V. C. Li, "Research on production, performance and fibre dispersion of PVA engineering cementitious

- composites,” *Materials Science and Technology*, vol. 25, no. 5, pp. 651–656, 2009.
- [23] S. L. Xu and X. R. Cai, “Experimental study on mechanical properties of ultra high toughness fiber reinforced cementitious composite,” *Journal of Hydraulic Engineering*, vol. 40, no. 9, pp. 1055–1063, 2009.
- [24] V. C. Li, “Micromechanics-based durability study of polyvinyl alcohol-engineered cementitious composites (PVA-ECC),” *ACI Materials Journal*, vol. 101, no. 3, pp. 242–248, 2004.
- [25] V. C. Li, H.-C. Wu, M. Maalej, D. K. Mishra, and T. Hashida, “Tensile behavior of cement-based composites with random discontinuous steel fibers,” *Journal of the American Ceramic Society*, vol. 79, no. 1, pp. 74–78, 1996.
- [26] H. Q. Xue, Z. C. Deng, and J. H. Li, “Tensile performance and toughness of PVA fiber reinforced cementitious composites,” *Journal of Zhengzhou University (Engineering Science)*, vol. 30, no. 1, pp. 92–95, 2009.
- [27] G. Parra-Montesinos and J. K. Wight, “Seismic response of exterior RC column-to-steel beam connections,” *Journal of Structural Engineering*, vol. 126, no. 10, pp. 1113–1121, 2000.
- [28] G. Fischer and V. C. Li, “Intrinsic response control of moment-resisting frames utilizing advanced composite materials and structural elements,” *ACI Structural Journal*, vol. 100, no. 2, pp. 166–176, 2003.
- [29] V. C. Li, G. Fischer, and M. Lepech, “Shotcreting with ECC,” in *Proceedings CD*, W. Kusterle, Ed., pp. 1–16, Spritzbeton-Tagung, Tyrol, Austria, 2009.
- [30] ECC Technology Network, *Repair of Mitaka Dam*, ECC Technology Network, Penfield, NY, USA, 2005.
- [31] J.-h. Hu, M.-Q. Sun, J. Li, and Y.-j. Wang, “Mechanical performances and evolution of stiffness of thin-walled strain hardening cement-based composites pipes during cyclic loading,” *Construction and Building Materials*, vol. 184, pp. 400–407, 2018.
- [32] K. Zhao, W. Chen, D. Yang, W. Zhao, S. Wang, and W. Song, “Mechanical tests and engineering applicability of fibre plastic concrete used in tunnel design in active fault zones,” *Tunnelling and Underground Space Technology*, vol. 88, pp. 200–208, 2019.
- [33] N. Okano, “Development of a testing machine with a large tunnel lining model,” *Railway Technology Avalanche*, vol. 19, p. 110, 2007.
- [34] K. Yashiro, R. Hirata, N. Okano, and Y. Kojima, “Study on deformation and failure behavior of mountain tunnel linings which consist of various materials,” *Journal of Japan Society of Civil Engineers, Ser. F1 (Tunnel Engineering)*, vol. 71, no. 2, pp. 78–94, 2015.
- [35] W. Z. Yuan, *Similarity Theory and Static Model Test*, Southwest Jiaotong University Press, Chengdu, China, 1998.
- [36] P. Feng, H. L. Qiang, and L. P. Ye, “Discussion and definition on yield points of materials, members and Structures,” *Engineering Mechanics*, vol. 34, no. 3, pp. 36–46, 2017.
- [37] P. Feng, S. Cheng, Y. Bai, and L. Ye, “Mechanical behavior of concrete-filled square steel tube with FRP-confined concrete core subjected to axial compression,” *Composite Structures*, vol. 123, pp. 312–324, 2015.
- [38] J. Pan, C. Mo, L. Xu et al., “Seismic behaviors of steel reinforced ECC/RC composite columns under low-cyclic loading,” *Journal of Southeast University (English Edition)*, vol. 33, no. 1, pp. 70–78, 2017.
- [39] O. Arnau and C. Molins, “Experimental and analytical study of the structural response of segmental tunnel linings based on an in situ loading test. Part 2: numerical simulation,” *Tunnelling and Underground Space Technology*, vol. 26, no. 6, pp. 778–788, 2011.
- [40] F. J. Vecchio and M. P. Collins, “The modified compression-field theory for reinforced concrete elements subjected to shear,” *ACI Journal Proceedings*, vol. 83, no. 2, pp. 219–231, 1986.
- [41] R. G. Selby and F. J. Vecchio, “Three-dimensional constitutive relations for reinforced concrete,” Report No. 93-02, University of Toronto, Toronto, Canada, 1993.
- [42] P. H. Feenstra, J. G. Rots, A. Amesen, J. G. Teigen, and K. V. Hoiseth, “A 3D constitutive model for concrete based on co-rotational concept,” in *Proceedings of the EURO-C 1998 Conference on Computational Modelling of Concrete Structures*, pp. 13–22, Rotterdam, Netherlands, 1998.
- [43] J. J. Zhou, J. L. Pan, and C. K. Y. Leung, “Mechanical behavior of fiber reinforced engineered cementitious composites in uniaxial compression,” *Journal of Materials in Civil Engineering*, vol. 27, no. 1, pp. 1–11, 2015.
- [44] F. Yuan, J. Pan, and C. K. Y. Leung, “Flexural behaviors of ECC and concrete/ECC composite beams reinforced with basalt fiber-reinforced polymer,” *Journal of Composites for Construction*, vol. 17, no. 5, pp. 591–602, 2013.
- [45] F. Yuan, J. Pan, and Y. Wu, “Numerical study on flexural behaviors of steel reinforced engineered cementitious composite (ECC) and ECC/concrete composite beams,” *Science China Technological Sciences*, vol. 57, no. 3, pp. 637–645, 2014.
- [46] *JTGD70-2014 Code for Design of Road Tunnel*, China Communications, Press, Beijing, China, 2014.

